

## MODELS FOR NONTHERMAL PHOTON SPECTRA

JOHN C. HOUCK AND GLENN E. ALLEN

MIT, Kavli Institute for Astrophysics and Space Research, 77 Massachusetts Avenue, Cambridge, MA 02139-4307

*Accepted for publication in ApJ Supplement*

### ABSTRACT

We describe models of nonthermal photon emission from a homogeneous distribution of relativistic electrons and protons. Contributions from the synchrotron, inverse Compton, nonthermal bremsstrahlung and neutral-pion decay processes are computed separately using a common parameterization of the underlying distribution of nonthermal particles. The models are intended for use in fitting spectra from multi-wavelength observations and are designed to be accurate and efficient. Although our applications have focused on Galactic supernova remnants, the software is modular, making it straightforward to customize for different applications. In particular, the shapes of the particle distribution functions and the shape of the seed photon spectrum used by the inverse Compton model are defined in separate modules and may be customized for specific applications. We assess the accuracy of these models by using a recurrence relation and by comparing them with analytic results and with previous numerical work by other authors.

*Subject headings:* radiation mechanisms: non-thermal — supernova remnants

### 1. INTRODUCTION

Cosmic-rays with energies up to about 1000 TeV are thought to be accelerated in supernova remnant shocks (Gaisser 1994). In the simplest, idealized model of the acceleration process, test particles interact with a shock discontinuity to produce a power-law momentum distribution of cosmic-rays. Photon spectra produced by power-law momentum spectra, as in the XSPEC models SRCUT and SRESC (Reynolds 1998; Reynolds & Keohane 1999), have been widely used to fit the X-ray synchrotron spectra of several SNRs.

However, in the diffusive shock acceleration picture (Blandford & Eichler 1987; Bell 1987; Ellison & Reynolds 1991; Berezhko & Ellison 1999), nonlinear processes are expected to cause some deviation, or curvature, away from a power-law momentum distribution. Recent observations of Cas A (Jones et al. 2003) and SN1006 (Allen, Houck & Sturmer 2005) have shown evidence for a curved synchrotron spectrum. Such spectra can be studied using simulations of diffusive shock acceleration in supernova remnants (see *e.g.* Ellison & Reynolds 1991; Baring et al. 1999; Bykov et al. 2000). These simulations predict the momentum distribution of nonthermal particles and the resulting photon emission spectrum. Unfortunately, such detailed calculations are still too time-consuming for widespread use in iterative fitting of models to observed spectra.

Therefore, we have developed models of the synchrotron (§3), inverse Compton (§4), nonthermal bremsstrahlung (§5) and neutral-pion decay (§6) spectra produced by homogeneous emitting regions having nonthermal particle momentum distributions with arbitrary shape. Our primary goals in developing these models were to make them as general and accurate as possible, and to make them computationally efficient enough to be practical for use in iterative fitting of observational data. An additional goal was to adhere to a modular design to simplify customizing the models for specific applica-

tions. By providing alternate implementations of the appropriate modules, one can customize the shapes of the particle distributions and the shape of the photon spectrum used to compute the inverse Compton model. For example, Allen, Houck & Sturmer (2005) used the synchrotron spectrum model with the curved particle momentum spectrum described in §2 to detect curvature in the cosmic-ray electron spectrum of SN1006.

We assess the accuracy of the computed photon spectra by applying a recurrence relation and by comparing with analytic results and with published numerical models (§7). When using these models to fit (§8) simultaneously radio, x-ray and gamma-ray observations of supernova remnants, we have occasionally found it useful to reduce the number of degrees of freedom by introducing additional physical constraints on the fit parameters. Gamma-ray spectra are particularly troublesome because they may contain significant contributions from inverse Compton emission, neutral-pion decay and nonthermal bremsstrahlung. By introducing additional physical constraints, one can usefully reduce the set of linear combinations of these models that fit the gamma-ray data. In §9, we discuss some of these constraints and describe how they may be imposed.

### 2. PARTICLE DISTRIBUTION FUNCTION

The algorithms used to compute the photon emission impose relatively few limitations on distribution functions suitable for use in fitting. The spectral models described below are derived assuming a particle momentum distribution function that depends only on the magnitude of the particle momentum and not its direction. For most practical applications, the momentum distribution function should depend on a reasonably small number of parameters and should be integrable by adaptive quadrature rules.

In applications to date, we have used a nonthermal particle distribution function of the form

$$N(p) = A \left( \frac{pc}{E_0} \right)^{-\Gamma + af(p)} \exp \left( \frac{E_0 - pc}{E_{\text{cutoff}}} \right), \quad (1)$$

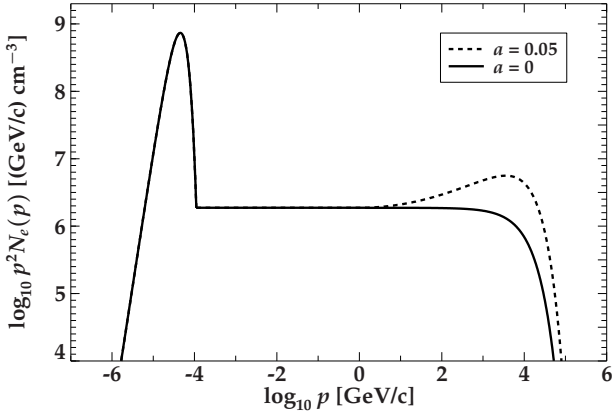


FIG. 1.— Sample electron momentum distribution function. At low energies, a Maxwellian thermal distribution ( $kT = 1$  keV) is shown. At high energies, two nonthermal distributions are shown, each with a high-energy exponential cutoff  $E_{\text{cutoff}} = 10$  TeV. The dashed line shows a nonthermal distribution with  $\Gamma = 2$  and with positive curvature ( $a = 0.05$ ) above momentum  $p = 1$  GeV/c. The other nonthermal component (solid line) has  $\Gamma = 2$  and zero curvature ( $a = 0$ ).

where

$$f(p) \equiv \begin{cases} \log(p/c/E_0), & p \geq E_0/c; \\ 0, & p < E_0/c, \end{cases} \quad (2)$$

and where  $p \equiv \gamma mv$ , and  $E_0 \equiv 1$  GeV. The same functional form is used for both protons and electrons. The normalization parameter,  $A$ , represents the density of particles with momentum  $p = E_0/c$  and has units  $\text{cm}^{-3}(\text{GeV}/c)^{-1}$ .

When  $a = 0$ , equation (1) describes a power-law distribution in momentum with an exponential cutoff at  $pc \approx E_{\text{cutoff}}$ . When  $a \neq 0$ , the power-law exponent changes with momentum for  $p \geq E_0/c$  (see Figure 1). The effect is such that, for each factor of ten increase in the momentum above  $E_0/c$ , the spectral index changes by an amount equal to the curvature parameter,  $a$ . Positive values of  $a$  cause the particle spectrum slope to flatten toward higher momenta, as shown in Figure 1. Positive values are expected due to nonlinear behavior of the diffusive acceleration mechanism (see *e.g.* Bell 1987; Ellison & Reynolds 1991; Berezhko & Ellison 1999). The qualitative effect of a small positive curvature on the shape of the nonthermal photon spectrum is shown in Figure 2.

Each of the photon emission models described below depends on parameters associated with the underlying momentum distribution of nonthermal particles. From equation (1), these parameters are  $\Gamma$ ,  $a$  and  $E_{\text{cutoff}}$ . The normalization parameter for each photon emission model includes the normalization parameter,  $A$ , for the relevant nonthermal particle distribution function.

The low end of the particle momentum distribution is dominated by a thermal Maxwellian as shown in Figure 1. As described in §9, one can impose charge conservation in the injection mechanism to set the value of the cosmic-ray proton normalization,  $A_p$  relative to the cosmic-ray electron normalization,  $A_e$ .

In computing nonthermal photon spectra, integrals over particle momenta generally include only relativis-

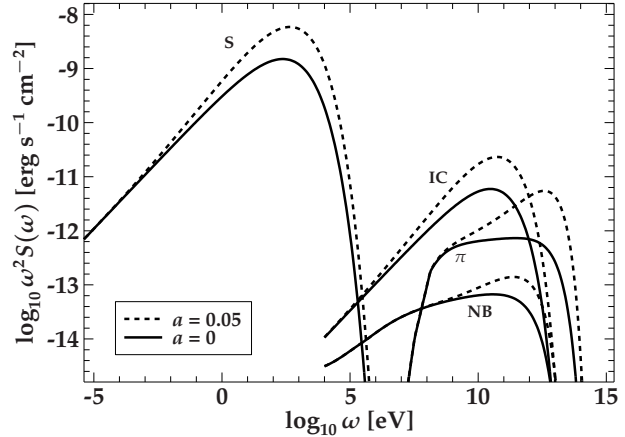


FIG. 2.— Example of the effect of curvature on nonthermal spectra. The solid lines show synchrotron (S), inverse Compton (IC), neutral-pion decay ( $\pi$ ) and nonthermal bremsstrahlung (NB) spectra with  $\Gamma = 2$  and no curvature ( $a = 0$ ). The dashed lines show the same spectra with positive curvature ( $a = 0.05$ ) above particle momentum  $p = 1$  GeV/c.

tic particles with  $\gamma \gg 1$ ; in practice, we use  $\gamma \geq 10$ .

### 3. SYNCHROTRON RADIATION

From Blumenthal & Gould (1970), the total synchrotron power emitted per unit frequency from an energetic electron ( $\gamma \gg 1$ ) spiraling in a magnetic field is

$$P_{\text{emitted}}(\nu) = \frac{\sqrt{3}e^3 B \sin \alpha}{m_e c^2} F\left(\frac{\nu}{\nu_c}\right), \quad (3)$$

where  $e$  is the electron charge,  $m_e$  is the electron mass,  $B$  is the magnetic field strength,  $\alpha$  is the pitch angle between the electron's velocity vector  $\mathbf{v}$  and the magnetic field vector  $\mathbf{B}$ ,  $\nu_c$  is the critical frequency, defined as

$$\nu_c = \frac{3eB\gamma^2}{4\pi m_e c} \sin \alpha \equiv \nu_0 \gamma^2 \sin \alpha, \quad (4)$$

and  $F(x)$ , the first synchrotron function, is defined as

$$F(x) \equiv x \int_x^\infty d\xi K_{5/3}(\xi), \quad (x \geq 0), \quad (5)$$

where  $K_{5/3}(\xi)$  is an irregular modified Bessel function. Note that equation (3) applies to frequencies well above the gyro-frequency, where the synchrotron spectrum may be regarded as continuous.

Assuming a steady state electron distribution, we define  $N(p, \alpha) dp d\Omega$  as the density of nonthermal electrons with pitch angles  $\alpha$  within a solid angle  $d\Omega$ , and momenta  $p$  within  $dp$ . From Blumenthal & Gould (1970),

$$\frac{dW}{dt} = \int dp \int d\Omega P_{\text{emitted}}(\nu) N(p, \alpha) \quad (6)$$

is the total synchrotron power received per unit volume and per unit frequency, integrated over pitch-angles.

Combining equations (3), (4) and (6), and assuming an isotropic distribution of pitch-angles so that  $N(p, \alpha) =$

$N(p)/4\pi$ , we obtain

$$\frac{dW}{d\nu dt} = \frac{\sqrt{3}e^3 B}{4\pi m_e c^2} \int dp N(p) \times \int_0^{2\pi} d\phi \int_0^\pi d\alpha \sin^2 \alpha F\left(\frac{\nu}{\nu_0 \gamma^2 \sin \alpha}\right), \quad (7)$$

Expressing this result in terms of a photon emission rate per unit energy, equation (7) yields the differential emissivity spectrum in the form

$$\frac{dn}{d\omega dt} = \frac{\sqrt{3}e^3 B}{h m_e c^2 \omega} \int dp N(p) R\left(\frac{\omega}{\omega_0 \gamma^2}\right), \quad (8)$$

where  $\omega$  is the photon energy and the angular integral is

$$R(x) \equiv \frac{1}{2} \int_0^\pi d\alpha \sin^2 \alpha F\left(\frac{x}{\sin \alpha}\right). \quad (9)$$

Crusius & Schlickeiser (1986) showed that equation (9) may be expressed analytically in terms of Whittaker functions,

$$R(x) = \frac{\pi x}{2} [W(x; 0, 4/3)W(x; 0, 1/3) - W(x; 1/2, 5/6)W(x; -1/2, 5/6)], \quad (10)$$

where  $W(z; \kappa, \mu) = e^{-z/2} z^{\mu+1/2} U(z; \frac{1}{2} + \mu - \kappa, 1 + 2\mu)$  and  $U(z; m, n)$  is a confluent hypergeometric function of the second kind.

The synchrotron flux is obtained by evaluating equation (8). To speed numerical computations, we compute  $R(x)$  using a cubic spline interpolation on a pre-computed table; we use the GNU Scientific Library (Galassi et al. 2005) to perform numerical integration and one-dimensional spline interpolation and to evaluate selected special functions. This table is constructed by evaluating equation (10) on an adaptive grid of  $x$  values chosen to accurately sample the behavior of the function over the range  $10^{-38} < x < 100$ . A log-spaced grid of  $x$  values was refined by adding interpolation points until the interpolated value of  $\log R(x)$  had a fractional error smaller than  $1.25 \times 10^{-5}$  at the midpoint of each  $x$  interval; we linearly interpolated the logarithms of  $x$  and  $R(x)$  only while refining the grid for the lookup table. In the final table, the associated cubic spline interpolation errors are  $|\delta R/R| \lesssim 5 \times 10^{-10}$  over the entire range of  $x$ .

The parameters of the synchrotron model are  $\Gamma$ ,  $a$ ,  $E_{\text{cutoff}}$ , the total magnetic field strength,  $B_{\text{tot}}$  and the normalization,

$$\mathcal{N}_S \equiv \frac{1}{4\pi d^2} \int_V dV A_e(r) = \frac{A_e V_S}{4\pi d^2}, \quad (11)$$

where  $A_e$  is the normalization of the nonthermal electron momentum distribution,  $d$  is the distance to the source and  $V_S$  is the synchrotron emitting volume. A homogeneous emitting volume is assumed.

Note that the parameters of the model describe the physical properties of the synchrotron-emitting plasma rather than the properties of the observed synchrotron emission. In some situations, two or more of the fit parameters are degenerate. For example, when fitting X-ray observations alone, the data constrain the critical frequency,  $\nu_c$ , but, because  $\nu_c$  depends on the product  $B_{\text{tot}} \gamma^2$ , the model parameters  $B_{\text{tot}}$  and  $E_{\text{cutoff}}$  are degenerate. Similarly, when fitting radio observations alone,

the normalization,  $\mathcal{N}_S$ , and  $B_{\text{tot}}$  are degenerate. In both cases, freezing  $B_{\text{tot}}$  solves the problem. Although one could group the physical parameters to remove degeneracies for special cases, we have chosen to keep the physical parameters separate. The advantage of this choice is that, by introducing additional observational constraints from other energy bands, it may be possible to constrain the physical parameters separately. For example, by fitting radio, X-ray and gamma-ray data simultaneously, one might individually constrain  $\mathcal{N}_S$ ,  $\Gamma$ ,  $a$ ,  $E_{\text{cutoff}}$  and  $B_{\text{tot}}$ .

#### 4. INVERSE COMPTON SCATTERING

Given a distribution of relativistic ( $\gamma \gg 1$ ) electrons  $N(p)$ , immersed in an isotropic radiation field with photon number density  $n(\omega_i)$ , the differential emissivity spectrum of Compton scattered photons for single-scattering is

$$\frac{dn}{d\omega dt} = c \int d\omega_i n(\omega_i) \int_{p_{\min}(\omega_i)}^{\infty} dp N(p) \sigma_{\text{KN}}(\gamma, \omega_i, \omega), \quad (12)$$

where  $\omega \equiv h\nu/(m_e c^2)$ , and

$$\sigma_{\text{KN}}(\gamma, \omega_i, \omega) = \frac{2\pi r_0^2}{\omega_i \gamma^2} \times \left[ 1 + q - 2q^2 + 2q \ln q + \frac{\Gamma^2 q^2 (1 - q)}{2(1 + \Gamma q)} \right] \quad (13)$$

is the Klein-Nishina scattering cross-section (Blumenthal & Gould 1970), where

$$q \equiv \frac{\omega}{4\omega_i \gamma (\gamma - \omega)}, \quad (14)$$

$\Gamma \equiv 4\omega_i \gamma$  and  $r_0 = e^2/(m_e c^2)$  is the classical electron radius.

The allowed range for  $q$  follows from the kinematics of Compton scattering. In the frame in which the electron is initially at rest, the incident photon has energy  $\omega'_i$  and the scattered photon energy may span the range  $\omega'_i/(1 + 2\omega'_i) \leq \omega' \leq \omega'_i$ . In the lab frame, the scattered photon energy lies in the range  $\omega_i \leq \omega \leq \Gamma/(1 + \Gamma)$ . Therefore, the allowed range for  $q$  is

$$q_{\min} \equiv \frac{1}{4\gamma(\gamma - \omega_i)} \leq q \leq 1. \quad (15)$$

The lower limit of the integral over electron momenta in equation (12) corresponds to the minimum electron momentum,  $p_{\min} = \gamma_{\min} m_e v$ , that can Compton scatter a photon from initial energy  $\omega_i$  to final energy  $\omega$ . From the kinematics, one can show that the threshold electron Lorentz factor is

$$\gamma_{\min} = \frac{1}{2} \left[ \omega + \sqrt{\omega^2 + \frac{\omega}{\omega_i}} \right], \quad (16)$$

which corresponds to  $q = 1$ .

The inverse Compton model is obtained by evaluating equation (12) for the cosmic background radiation field so that

$$n(\omega_i) = \frac{1}{\pi^2 \lambda^3} \frac{\omega_i^2}{e^{\omega_i/\Theta} - 1}, \quad (17)$$

where  $\lambda \equiv \hbar/(m_e c)$  is the electron Compton wavelength,  $\Theta \equiv kT/(m_e c^2)$ , and  $T = 2.725$  K (Bennett et al. 2003).

For computational convenience, it is useful to change the order of integration. Performing the integral over photon energies first, we let the electron momentum integral extend over the full range of electron momenta and use the cross-section

$$\sigma(\gamma, \omega_i, \omega) = \begin{cases} \sigma_{\text{KN}}(\gamma, \omega_i, \omega), & q_{\min} \leq q \leq 1; \\ 0, & \text{otherwise.} \end{cases} \quad (18)$$

We can then speed up numerical computations by tabulating the photon energy integral,

$$I_c(\omega, \gamma) \equiv \int d\omega_i n(\omega_i) \sigma_{\text{KN}}(\gamma, \omega_i, \omega), \quad (19)$$

for a given spectrum of seed photons,  $n(\omega_i)$ . In practice, we use  $q$  as the variable of integration to evaluate the integral in equation (19).

Because the range of  $I_c(\omega, \gamma)$  spans many orders of magnitude over the domain of interest, we find it useful to interpolate on the logarithm of the function value. In constructing an interpolation table for  $I_c(\omega, \gamma)$ , we explicitly incorporate the existence of the threshold Lorentz factor  $\gamma_{\min}$ . Because  $I_c(\omega, \gamma)$  asymptotically goes to zero as  $\gamma \rightarrow \gamma_{\min}$ , we set  $I_c(\omega, \gamma) = 0$  for  $\gamma < \gamma_0 \equiv \gamma_{\min}(\omega_{i,\max})$  where  $\omega_{i,\max}$  is the maximum incident photon energy of interest. Introducing a change of variables,  $x_c \equiv \log(\log(\gamma/\gamma_0))$  and  $y_c \equiv \log \omega$ , we tabulate  $\log I_c(x_c, y_c)$  on a  $1024 \times 1024$  uniform rectangular grid in  $x_c$  and  $y_c$  covering the range  $10 \leq \gamma \leq 10^{9.5}$  and  $10^2 \leq \omega \leq 10^{15}$  eV. The smoothness of the resulting table allows accurate two-dimensional interpolation with a 6<sup>th</sup>-order spline (de Boor 1978) in each coordinate.

The parameters of the inverse Compton model are  $\Gamma$ ,  $a$ ,  $E_{\text{cutoff}}$ , the blackbody temperature,  $T$  and the normalization,

$$\mathcal{N}_I \equiv \frac{1}{4\pi d^2} \int_V dV A_e(r) = \frac{A_e V_I}{4\pi d^2}, \quad (20)$$

where  $V_I$  is the homogeneous emitting volume. By default, the temperature parameter,  $T$ , is not used and the model uses a lookup table for  $I_c(\omega, \gamma)$  appropriate for seed photons from the cosmic background radiation field. The error associated with interpolation in this table is typically  $|\delta I_c/I_c| < 10^{-10}$ .

A switch is provided to force the model to compute the radiation field integral by direct integration instead of table interpolation. The computational expense of direct integration currently makes this mode impractical for use in spectral fitting.

Alternatively, one can use a linear combination of lookup tables to describe a more complicated radiation field. For example, one can construct lookup tables corresponding to a dilute stellar radiation field or to emission from molecular clouds. During the fit, one can vary the relative proportions of these components. Note that the current implementation restricts the input radiation field shape to one that is integrable by adaptive quadrature rules.

The inverse Compton emitting volume,  $V_I$ , need not be the same as the synchrotron emitting volume,  $V_S$ . Because the cosmic background radiation photons will fill the entire synchrotron emitting volume,  $V_I$  will usually be at least as large as  $V_S$ . However, if nonthermal electrons are found in a volume with a relatively weak magnetic

field, that volume will produce inverse Compton emission, but little synchrotron emission, and  $V_I > V_S$ . For this reason, it is useful to allow the inverse Compton and synchrotron norms to be different.

## 5. NONTHERMAL BREMSSTRAHLUNG

In this section, we consider nonthermal bremsstrahlung emission from a population of nonthermal electrons incident on a stationary target containing free electrons and ions. The total bremsstrahlung emissivity is computed as a sum of contributions from electron-electron and electron-ion bremsstrahlung.

Given two populations of relativistic particles with momentum distributions,  $N_1(p_1)$  and  $N_2(p_2)$ , and with interaction cross-section,  $\sigma$ , the general expression for the collision rate per unit volume is

$$\frac{dn}{dt} = (1 + \delta_{12})^{-1} \int dp_1 N_1(p_1) \int dp_2 N_2(p_2) \times \sigma \sqrt{(\mathbf{v}_1 - \mathbf{v}_2)^2 - (\mathbf{v}_1 \times \mathbf{v}_2)^2/c^2}, \quad (21)$$

where the integrals extend over the momenta of the interacting distributions (Landau & Lifshitz 1975). The Kronecker delta,  $\delta_{12}$  corrects for double-counting when the particles are identical.

When  $|\mathbf{v}_2| \ll |\mathbf{v}_1|$ , equation (21) reduces to the familiar non-relativistic form, and one of the populations may be treated as a stationary target. For example, when the target particles may be characterized by a Maxwellian thermal distribution, the thermal motions of the target particles may be neglected as long as  $kT_2 \ll (\gamma - 1)mc^2$ .

### 5.1. Electron-Electron Bremsstrahlung

In the limit that  $|\mathbf{v}_2| \ll |\mathbf{v}_1|$ , equation (21) yields a differential emissivity spectrum for electron-electron bremsstrahlung of the form

$$\frac{dn}{d\omega dt} = n_e \int dp N(p) v \frac{d\sigma_{ee}}{d\omega}, \quad (22)$$

where  $n_e$  is the target electron density, and  $d\sigma_{ee}/d\omega$  is the lab-frame differential cross-section for this interaction between identical particles and includes the factor  $(1 + \delta_{12})^{-1}$ .

The lab-frame cross-section,  $d\sigma_{ee}/d\omega d\psi$ , differential in both photon energy,  $\omega$ , and photon emission angle,  $\psi$  was taken from Haug (1975) and was computed using software kindly provided by E. Haug. The lab-frame cross-section, differential in photon energy,  $d\sigma_{ee}/d\omega$ , is obtained by integrating over photon emission angles. The angular integration limits are given by Haug (1975) and follow from energy-momentum conservation. In the center of momentum (CM) frame, the photon emission is symmetric along the direction of motion and all values of  $\psi_*$  are accessible. For an electron incident with momentum  $p = \gamma mv$  in the lab frame, beaming restricts photon emission angles to a narrow cone in the forward direction. From Haug (1975), photons with energies  $(\gamma - 1)/(\gamma + \gamma\beta + 1) < \omega \leq (\gamma - 1)/(\gamma - \gamma\beta + 1)$  are emitted into a cone with the maximum emission angle,  $\psi_{\max}$ , given by

$$\cos \psi_{\max} = \frac{(\gamma + 1)\omega - (\gamma - 1)}{\omega\gamma\beta}. \quad (23)$$

Lower energy photons may span  $0 \leq \psi \leq \pi$ .

In carrying out the angular integration for ultra-relativistic electrons, some care must be taken to minimize numerical problems due to round-off errors. In particular, the expression for the differential cross-section,  $d\sigma_{ee}/d\omega d\psi$ , includes terms that divide by the quantity

$$x = \omega(E - p \cos \psi), \quad (24)$$

where  $E \equiv T + 1$ ,  $p \equiv \sqrt{T(T+2)}$ , and  $T$  is the incident electron kinetic energy in units of  $m_e c^2$ . For  $\gamma > 10^8$ ,  $x$  is identically zero in double-precision for  $\cos \psi = 1$ , causing a division by zero error. In the ultra-relativistic regime, we computed  $x$  using the first few terms of its series expansion in powers of  $\gamma^{-2}$ . Substituting  $\cos \psi \equiv 1 - s$ , and using  $s$  as the variable of integration, the relevant cancellations can be handled analytically. To check the result, we used the Lorentz invariant,  $\omega d^3\sigma/dp^3$ , to transform Haug's CM-frame cross-section into the lab frame (see *e.g.* Dermer 1986). In the CM frame, the cross-section computation is less affected by round-off errors because the relevant electron Lorentz factor is  $\gamma_e = ((\gamma+1)/2)^{1/2}$ . Applying the Lorentz transformation and treating round-off errors by handling the relevant cancellations analytically, we verified that the transformed result agreed with the lab-frame cross-section in the ultra-relativistic regime.

To speed up the numerical integrations, the cross-section is evaluated using a two-dimensional cubic-spline interpolation on pre-computed tables. In constructing an interpolation table for  $d\sigma_{ee}/d\omega \equiv \sigma'$ , we explicitly incorporate the fact that  $\sigma'(T, \omega) \equiv 0$  for kinetic energies  $T < T_{\min}(\omega)$ , where  $T_{\min}(\omega)$  is determined by the kinematics. We define  $T_{\min}(\omega)$  numerically as the locus of points at which  $\sigma'(T_{\min}, \omega) = \epsilon_B \max\{\sigma'(T, \omega)\}$  for  $\epsilon_B = 10^{-8}$ . Introducing a change of variables,  $x_B \equiv \log(\log(T/T_{\min}))$  and  $y_B \equiv \log \omega$ , we tabulate  $\log \sigma'(x_B, y_B)$  on a  $1024 \times 1024$  rectangular grid in  $x_B$  and  $y_B$  covering  $10^2 \leq T/mc^2 \leq 10^{9.5}$  and  $10^2 \leq \omega/mc^2 \leq 10^{9.5}$ . The smoothness of the resulting table allows accurate two-dimensional cubic spline interpolation. The error associated with interpolation in the cross-section table is  $|\delta\sigma'/\sigma'| < 10^{-5}$ .

## 5.2. Electron-Ion Bremsstrahlung

From equation (21) the differential emissivity spectrum for electron-ion bremsstrahlung can be written

$$\frac{dn}{d\omega dt} = n_Z \int dp N(p) v \frac{d\sigma_{eZ}}{d\omega}, \quad (25)$$

where  $n_Z$  is the density of target ions with charge  $Z$ , and  $d\sigma_{eZ}/d\omega$  is the lab-frame differential cross-section.

The Bethe-Heitler cross-section (Heitler 1953; Koch & Motz 1959) determines the probability that deflection of a relativistic electron in the unscreened field of an ion of charge  $Z$  will yield a photon of energy  $\omega = h\nu/(m_e c^2)$ . The differential cross-section may be written in the form

$$\frac{d\sigma_{eZ}}{d\omega} = \frac{\bar{\phi}}{\omega} \frac{\gamma \beta}{\gamma_0 \beta_0} \left[ \frac{4}{3} - \frac{2\gamma_0 \gamma (\gamma_0^2 \beta_0^2 + \gamma^2 \beta^2)}{\gamma_0^2 \gamma^2 \beta_0^2 \beta^2} \right. \\ \left. + \frac{a_0 \gamma}{\gamma_0^3 \beta_0^3} + \frac{a \gamma_0}{\gamma^3 \beta^3} - \frac{a_0 a}{\gamma_0 \gamma \beta_0 \beta} + Lx \right], \quad (26)$$

where

$$x \equiv \frac{8}{3\beta_0 \beta} + \frac{\omega^2(1 + \beta_0^2 \beta^2)}{\gamma_0 \gamma \beta_0^3 \beta^3} + \frac{\omega}{2\gamma_0 \gamma \beta_0 \beta} \\ \times \left[ \frac{a_0(\gamma + \gamma_0 \beta_0^2)}{\gamma_0^2 \beta_0^3} - \frac{a(\gamma_0 + \gamma \beta^2)}{\gamma^2 \beta^3} + \frac{2\omega}{\gamma_0 \gamma \beta_0^2 \beta^2} \right], \quad (27)$$

$$\bar{\phi} \equiv \alpha Z^2 r_0^2, \quad r_0 = e^2/(m_e c^2), \quad (28)$$

$$a_0 \equiv 2 \ln [\gamma_0 (1 + \beta_0)], \quad a \equiv 2 \ln [\gamma (1 + \beta)], \quad (29)$$

$$L \equiv 2 \ln [(\gamma_0 \gamma + \gamma_0 \gamma \beta_0 \beta - 1) / \omega]. \quad (30)$$

In these expressions,  $\alpha$  is the fine structure constant and  $\gamma(\beta)$  and  $\gamma_0(\beta_0)$  are the Lorentz factors of the scattered and incident electron, respectively. The Bethe-Heitler cross-section is derived using the Born approximation which is appropriate in the limit of high kinetic energies, such that  $2\pi\alpha Z/\beta \ll 1$  for both the incident and scattered electron. The recoil of the nucleus is neglected so  $\gamma_0(\beta_0) = \gamma(\beta) + \omega$ . The accuracy at low energies is improved by including the Elwert correction factor, which we apply at all energies (Elwert 1939; Pratt & Tseng 1975; Haug 1997), so that  $d\sigma_{eZ}/d\omega \rightarrow \eta_E d\sigma_{eZ}/d\omega$  where

$$\eta_E \equiv \frac{\xi}{\xi_0} \frac{1 - \exp(-\xi_0)}{1 - \exp(-\xi)}, \quad (31)$$

and where

$$\xi \equiv 2\pi\alpha \frac{Z}{\beta}, \quad \xi_0 \equiv 2\pi\alpha \frac{Z}{\beta_0}. \quad (32)$$

When the target ions retain bound atomic electrons, it is necessary to modify the cross-section to account for screening of the nuclear charge. We assume that the target material is completely ionized so that screening corrections are not necessary.

The relative simplicity of the cross-section makes it practical to perform the integration over electron momenta by evaluating (26) directly rather than interpolating values from a pre-computed table.

The parameters of the nonthermal bremsstrahlung model are  $\Gamma$ ,  $a$ ,  $E_{\text{cutoff}}$  and the normalization,

$$\mathcal{N}_B \equiv \frac{1}{4\pi d^2} \int_V dV n_0(r) A_e(r) = \frac{A_e n_0 V_B}{4\pi d^2}, \quad (33)$$

where  $n_0 \equiv \sum_Z n_Z$  is the total ion number density of the target,  $n_Z$  is the number density of ions with charge  $Z$  and  $V_B$  is the emitting volume. The user interface includes parameters to control the relative contributions of electron-electron and electron-proton bremsstrahlung. The electron-electron contribution has weight  $X_e \equiv \sum_Z Z n_Z / n_0$  and the electron-proton contribution has weight  $X_i \equiv \sum_Z Z^2 n_Z / n_0$ . By default, the target is assumed to consist of hydrogen and helium with  $n_{\text{He}}/n_{\text{H}} = 0.1$  so that the default weights are  $X_e = X_{\text{H}} + 2X_{\text{He}} = 1.091$  and  $X_i = X_{\text{H}} + 4X_{\text{He}} = 1.273$ . A common alternative is to view  $n_0$  as the target proton density and to compute the weights using that assumption. As long as the weights are consistent with the definition of  $n_0$ , the result is the same.

## 6. NEUTRAL PION DECAY

Nonthermal protons produce gamma-ray emission primarily through collisions with thermal protons. These collisions yield neutral pions via  $pp \rightarrow \pi^0 + X$ , and the neutral pions decay via  $\pi^0 \rightarrow 2\gamma$ . We include only the contribution from proton-proton collisions and ignore contributions from processes other than the decay of neutral pions. In its rest-frame, the neutral pion decays within  $\sim 10^{-16}$  sec, producing two gamma-rays, each with an energy of  $\omega_0 = \frac{1}{2}m_\pi c^2$ . Because the pion has zero spin, the gamma-rays are emitted isotropically. Following Hillier (1984), the number of gamma-rays emitted into a rest frame angle between  $\theta_*$  and  $\theta_* + d\theta_*$  is

$$n(\theta_*)d\theta_* = \sin \theta_* d\theta_*. \quad (34)$$

Since a gamma-ray that is emitted at an angle  $\theta_*$  in the pion rest frame has a lab-frame energy

$$\omega = \omega_0 \gamma_\pi (1 - \beta_\pi \cos \theta_*), \quad (35)$$

the number of gamma-rays with lab-frame energy between  $\omega$  and  $\omega + d\omega$  is

$$n(\omega) = n(\theta_*) \frac{d\theta_*}{d\omega} = \frac{1}{\omega_0 \gamma_\pi \beta_\pi} = \frac{2}{p_\pi c}, \quad (36)$$

where  $p_\pi = \gamma_\pi m_\pi v_\pi$  is the pion momentum. For a population of pions with momentum distribution,  $N_\pi(p_\pi)$ , the gamma ray spectrum is then

$$n(\omega) = 2 \int_{p_{\pi,\min}}^{p_{\pi,\max}} N_\pi(p_\pi) \frac{dp_\pi}{p_\pi}. \quad (37)$$

The lower integration limit is set by the minimum pion momentum required to yield a lab-frame photon of energy  $\omega$ . From equation (35), the low energy gamma-ray has energy  $\omega_{\min} = \omega_0 \gamma_\pi (1 - \beta_\pi)$ , corresponding to a pion velocity of

$$\beta_{\pi,\min} = \frac{\omega_0^2 - \omega^2}{\omega_0^2 + \omega^2}. \quad (38)$$

A lab frame photon of energy  $\omega$  therefore requires a pion Lorentz factor of at least

$$\gamma_{\pi,\min} = \frac{1}{2} \left( \frac{\omega}{\omega_0} + \frac{\omega_0}{\omega} \right). \quad (39)$$

The upper integration limit corresponds to the maximum pion momentum that can be produced by a proton of kinetic energy  $T_{p,\max}$ . From the collision kinematics, one can show that

$$\gamma_{\pi,\max} = \frac{1}{2} \left( \frac{T_{p,\max}}{2\omega_0} + \frac{\omega_0}{m_p c^2} \right). \quad (40)$$

The production spectrum of secondary pions in proton-proton collisions is

$$N_\pi(p_\pi) = n_p \int_{p_{\min}(p_\pi)}^{\infty} dp v_p N_p(p) \frac{d\sigma(p_\pi, p)}{dp_\pi}, \quad (41)$$

where  $n_p$  is the density of target protons,  $v_p$  is the non-thermal proton velocity,  $N_p(p)$  is the nonthermal proton momentum distribution, and  $d\sigma(p_\pi, p)/dp_\pi$  is the differential cross-section for production of a neutral pion with lab-frame momentum  $p_\pi$  from a proton with lab-frame momentum  $p$ . The lower integration limit is the threshold proton momentum for producing a pion with

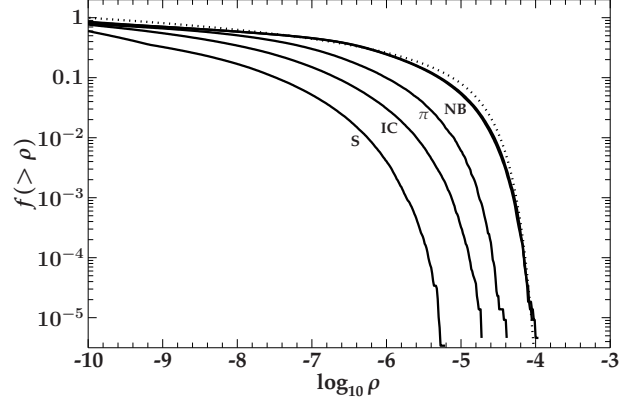


FIG. 3.— Distribution of fractional recurrence relation errors. The fraction,  $f$ , of errors larger than  $\rho$ , is shown for each spectral model. The errors were computed at many points along each of several model spectra. One spectrum was generated for each pair of values,  $\Gamma$  and  $E_{\text{cutoff}}$ , over a grid spanning  $1.8 \leq \Gamma \leq 4$  and  $1 \leq E_{\text{cutoff}} \leq 1000$  TeV. The dotted line corresponds to  $f(> \rho) = \exp(-\rho^2/2\sigma^2)$ , with  $\sigma = 2.5 \times 10^{-5}$ . Note that the curves for electron-electron and electron-proton bremsstrahlung are almost identical.

momentum  $p_\pi$ . From the collision kinematics, one can show that the threshold proton kinetic energy is

$$T_{p,\min}(p_\pi) = 2 (p_\pi^2 c^2 + m_\pi^2 c^4)^{1/2} + \frac{m_\pi^2 c^2}{2m_p}. \quad (42)$$

For the purpose of interactive spectral fitting, computing the photon spectrum from neutral-pion decay by direct integration over the proton momentum distribution and over the resulting pion spectrum is quite computationally demanding. The cost of the numerical integrations is compounded by the fact that the differential cross-sections are computationally expensive for certain energies (see *e.g.* Dermer 1986; Mori 1997). To reduce the cost of these computations, we evaluate the integral over the proton distribution using the delta-function approximation described by Aharonian & Atoyan (2000).

The parameters of the neutral-pion decay model are  $\Gamma$ ,  $a$ ,  $E_{\text{cutoff}}$  and the normalization,

$$\mathcal{N}_\pi \equiv \frac{1}{4\pi d^2} \int_V dV n_p(r) A_p(r) = \frac{A_p n_p V_\pi}{4\pi d^2}, \quad (43)$$

where  $A_p$  is the normalization for the nonthermal proton momentum distribution,  $n_p$  is the density of target protons, and  $V_\pi$  is the emitting volume. Note that for this model, the parameters  $\Gamma$ ,  $a$  and  $E_{\text{cutoff}}$  refer to the proton momentum distribution.

## 7. ACCURACY OF COMPUTED SPECTRA

Consider spectral models of the form

$$S_\Gamma(\omega; \varepsilon_c) = \int dp \left( \frac{p}{\varepsilon_0} \right)^{-\Gamma} \exp \left( \frac{\varepsilon_0 - p}{\varepsilon_c} \right) \phi(p, \omega), \quad (44)$$

where  $\omega$  is the photon energy,  $p$  is the particle momentum,  $\varepsilon_0$  is a scaling constant, and  $\phi(p, \omega)$  depends on the physical process. Taking the derivative with respect to  $1/\varepsilon_c \equiv \alpha$ , we find that

$$\frac{1}{\varepsilon_0} \frac{dS_\Gamma(\omega; \alpha)}{d\alpha} = S_\Gamma(\omega; \alpha) - S_{\Gamma-1}(\omega; \alpha). \quad (45)$$

This identity specifies a recurrence relation between spectra of the form shown in equation (44).

Numerical evaluation of equation (44) yields model spectra of the form  $S_\Gamma(\omega; \alpha) + \Lambda(\omega; \alpha, \Gamma)$ , where  $S_\Gamma$  is the exact result and  $\Lambda$  represents the error in the computation. Because accurately computed spectra must satisfy equation (45), it follows that  $\Lambda(\omega; \alpha, \Gamma)$  must also satisfy equation (45). Although an error in the computation of  $\phi(p, \omega)$  might generate such  $(\alpha, \Gamma)$  dependent errors in the computed spectrum, such an error should be detectable on comparison with an analytic solution or with an independent numerical calculation. Eliminating that possibility, the error term in computed spectra that satisfy equation (45) must be independent of  $\alpha$  and  $\Gamma$  so that  $\Lambda(\omega; \alpha, \Gamma) = \Lambda(\omega)$ . The magnitude of the energy-dependent error,  $\Lambda(\omega)$  must be estimated by other means, such as by comparing with analytic solutions and with independent numerical results. Although satisfying the recurrence relation does not prove that the spectral computations are correct, it does provide strong constraints on the magnitude and parameter dependence of the error term,  $\Lambda$ .

To verify equation (45) numerically, we introduce a finite-difference approximation for the derivative. It follows that computed spectra of the form shown in equation (44) should obey a relationship of the form  $\mathcal{R}(\omega; \Gamma, \alpha) = 0$  where

$$\begin{aligned} \mathcal{R}(\omega; \Gamma, \alpha) &\equiv 1 - \frac{S_{\Gamma-1}(\alpha)}{S_\Gamma(\alpha)} \\ &- \lim_{\delta\alpha \rightarrow 0} \frac{S_\Gamma(\alpha + \delta\alpha/2) - S_\Gamma(\alpha - \delta\alpha/2)}{S_\Gamma(\alpha)\varepsilon_0\delta\alpha}. \end{aligned} \quad (46)$$

For clarity in equation (46), we have avoided writing out the explicit dependence of the right-hand side upon photon energy,  $\omega$ . The centered difference used to approximate the derivative in equation (46) should yield quadratic convergence in the limit that  $\delta\alpha \rightarrow 0$ . For each of our spectral models, we verified that, in the limit  $\delta\alpha \rightarrow 0$ ,  $\mathcal{R} \rightarrow 0$  as  $\mathcal{R} \propto (\delta\alpha)^2$ ; observing smooth convergence at the expected rate confirms that the models behave as expected. In subsequent evaluations of equation (46), we adopt a value of  $\delta\alpha/\alpha = 2.5 \times 10^{-6}$ . Because individual terms in equation (46) can be  $\gg 1$ , it is useful to compute the fractional error,  $\rho \equiv |\mathcal{R}|/|\mathcal{R}|$ , where the denominator is the  $\ell^2$ -norm of the three terms in equation (46).

To test the  $\Gamma$  and  $\alpha$  dependence of  $\Lambda$ , we computed values of  $\rho$  at many points along each of several spectra. One spectrum was computed for each pair of  $(\Gamma, \alpha)$  values on a grid sampling the range  $1.8 \leq \Gamma \leq 4$  and  $1 \leq E_{\text{cutoff}} \leq 1000$  TeV. For the synchrotron model,  $\rho$  was evaluated at photon energies in the range  $10^{-5} \text{ eV} \leq \omega \leq 10^5 \omega_c$ , where  $\omega_c$  is the critical energy. For the other models,  $\rho$  was evaluated at photon energies in the range  $10^5 \text{ eV} \leq \omega \leq 3E_{\text{cutoff}}$ . Each photon energy grid was logarithmically spaced and used 80 points per decade. Figure 3 shows that, throughout this range,  $\rho$  was  $\lesssim 10^{-4}$ . We conclude that, throughout the parameter range of interest, the  $(\alpha, \Gamma)$  dependence of  $\Lambda$  is no larger than about a part in  $10^4$ . This result suggests that the errors are essentially independent of the parameters of the particle distribution function.

To test the dependence of the errors on the other pa-

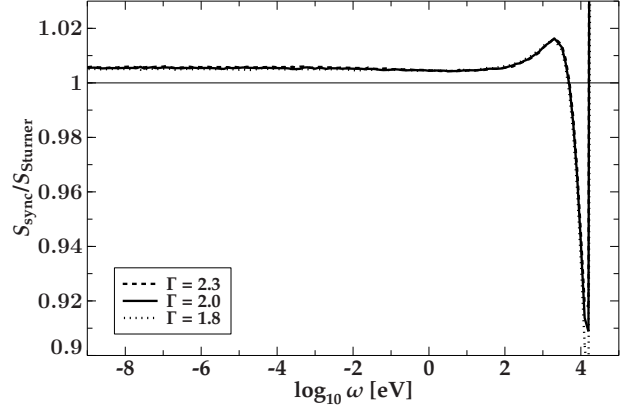


FIG. 4.— Ratio showing our synchrotron models divided by those of Sturner et al. (1997) for  $\Gamma = 1.8$  (dashed),  $\Gamma = 2$  (solid), and  $\Gamma = 2.3$  (dotted). Note that the three curves are almost identical.

rameters, including the photon energy, we compare our results with other analytic and numerical solutions. Blumenthal & Gould (1970) derive the well-known analytic result that the synchrotron spectrum from a power-law distribution of electrons,  $N(\gamma) \propto \gamma^{-\Gamma}$ , is itself a power-law of the form  $S(\nu) \propto \nu^{-(\Gamma-1)/2}$ . To compare with this result, we used a power-law electron distribution function to compute numerically  $S_{\text{sync}}(\nu) \equiv \omega dn/d\omega dt$ , as described above in equation (8), and we computed  $S(\nu) \equiv dW/d\nu dt$  from equation (4.59) of Blumenthal & Gould (1970). In deriving the analytic solution, the lower limit of the integral over  $\gamma$  is extended to zero (Blumenthal & Gould 1970), effectively neglecting the electron mass. Consistent with this assumption, the value of  $x = \nu/\nu_c$  in the numerical integrand must be computed using the approximation  $\gamma \approx p/(m_e c)$  otherwise, the computed spectrum departs from the analytic solution at low frequencies. We find that the absolute value of the fractional error is

$$|\epsilon_{\text{sync}}| \equiv \left| 1 - \frac{S_{\text{sync}}(\nu)}{S(\nu)} \right| < 3 \times 10^{-11}, \quad (47)$$

for frequencies in the range  $10^7 \leq \nu \leq 10^{20} \text{ Hz}$  and for values of  $\Gamma$  and  $B_{\text{tot}}$  in the ranges  $1 \leq \Gamma \leq 4$  and  $1 \leq B_{\text{tot}} \leq 10^4 \mu\text{G}$ , respectively. The primary source of error in this comparison is associated with interpolation of  $R(x)$  in our precomputed table; computing  $R(x)$  directly in terms of hypergeometric functions, we reproduce the analytic solution to within  $|\epsilon_{\text{sync}}| < 3 \times 10^{-13}$  over the specified range of  $\nu$ ,  $\Gamma$  and  $B_{\text{tot}}$ .

Blumenthal & Gould (1970) also discuss the inverse Compton spectrum produced by a power-law distribution of electrons scattering photons from a blackbody radiation field. They give asymptotic analytic solutions valid in the Thomson limit and in the extreme Klein-Nishina limit. To compare our inverse Compton model with these analytic solutions, we used a power-law electron distribution function,  $N(\gamma) \propto \gamma^{-\Gamma}$ , to compute numerically  $s_{\text{inv}}(\omega) \equiv dn/d\omega dt$ , as described above in equation (12). For the purpose of these tests, we evaluated the integral over incident photon energies (equation 19) by direct numerical integration rather than by spline interpolation in precomputed tables.

In the Thomson limit, the energy of the incident photon in the electron rest frame is small compared to the

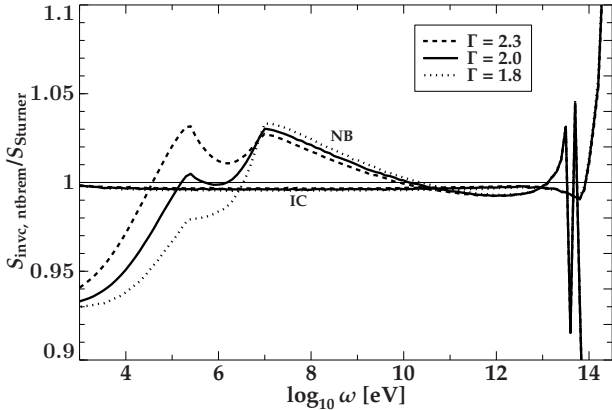


FIG. 5.— Ratio showing our inverse Compton and nonthermal bremsstrahlung spectra divided by those of Sturner et al. (1997) for  $\Gamma = 1.8$  (dashed),  $\Gamma = 2$  (solid), and  $\Gamma = 2.3$  (dotted). The three curves for the inverse Compton spectra are almost identical.

electron rest energy and the momentum transferred by the electron is small compared to its initial momentum. In this regime, corresponding to  $\omega_i \ll \omega \ll \gamma mc^2$ , the scattering cross-section is essentially independent of the energy of the incoming photon. The Thomson limit approximation is most accurate in the limit of low radiation temperature,  $T$ , and for scattered photon energies near the middle of the applicable energy range. Such a case provides the best test of the accuracy of our inverse Compton model in the Thomson limit. For power-law slopes in the range  $1 \leq \Gamma \leq 4$  and radiation field temperatures  $10^{-2} \leq T \leq 10^4$  K, we used our model to compute inverse Compton spectra,  $s_{\text{invc}}(\omega)$ , for scattered photon energies in the range  $10\gamma_{\min}^2 kT \leq \omega \leq 0.1\gamma_{\min} mc^2$ , using  $\gamma_{\min} \equiv 10$ . For comparison, we computed  $s(\omega) \equiv dN_{\text{tot}}/dtde_1 \propto \omega^{-(\Gamma+1)/2}$  using equation (2.65) of Blumenthal & Gould (1970). We found that our inverse Compton model converged smoothly to the analytic result in the appropriate limit. The smallest fractional difference is

$$|\epsilon_{\text{invc}}| \equiv \left| 1 - \frac{s_{\text{invc}}(\omega)}{s(\omega)} \right| < 10^{-8}. \quad (48)$$

Broader comparisons are less useful as a test of computational accuracy because the asymptotic solution itself becomes less accurate with increasing  $T$  and for energies approaching the endpoints of the applicable range. For  $T = 0.01$  K, the fractional error is smallest ( $|\epsilon_{\text{invc}}| < 10^{-8}$ ) at  $\omega \approx 50$  eV, then increases toward lower and higher energies with  $|\epsilon_{\text{invc}}| < 10^{-3}$  for the range  $10^{-2} \leq \omega \leq 10^7$  eV. Increasing  $T$  narrows the applicable energy range so that for  $T = 10^4$  K,  $|\epsilon_{\text{invc}}| < 10^{-3}$  only for the range  $2 \lesssim \omega \lesssim 5$  keV.

In the extreme Klein-Nishina limit, the energy of the incident photon in the electron rest frame is large compared to the electron rest energy. In this regime, corresponding to  $\omega_i\gamma \gg mc^2$ , the scattering cross-section is strongly peaked near the maximum scattered photon energy so that individual Compton scatterings tend to involve a large energy transfer. The characteristic scattered photon energy is then  $\omega \sim \gamma mc^2$ . It follows that this regime may be characterized by the requirement that  $\omega_i\omega \gg m^2c^4$  so that, for a black-body radiation field with  $\omega_i \sim kT$ , the extreme Klein-

Nishina limit corresponds to scattered photon energies  $\omega \gg m^2c^4/(kT)$ . We computed  $s(\omega) \equiv dN_{\text{tot}}/dtde_1$  using equation (2.88) of Blumenthal & Gould (1970)<sup>1</sup>. In the extreme Klein-Nishina limit, we computed inverse Compton spectra,  $s_{\text{invc}}(\omega)$ , for scattered photon energies in the range  $10^3 m^2 c^4/(kT) \leq \omega \leq 10^{12} m^2 c^4/(kT)$  for power-law slopes in the range  $1 \leq \Gamma \leq 4$  and radiation field temperatures in the range  $T = 10^3 - 10^8$  K. We found that the inverse Compton model spectra converged smoothly to the analytic result,  $s(\omega)$ . The fractional error decreased smoothly with increasing photon energy from  $|\epsilon_{\text{invc}}| \approx 10^{-3}$  at  $\omega \approx 10^3 m^2 c^4/(kT)$  to  $|\epsilon_{\text{invc}}| \approx 3 \times 10^{-8}$  for  $\omega \approx 10^9 m^2 c^4/(kT)$ . Numerical round-off errors become important at higher energies.

To examine the absolute accuracy of our computed photon spectra for more realistic particle spectra, we compared our results with those of Sturner et al. (1997). To facilitate this comparison, Sturner kindly computed photon spectra for a particle distribution function of the form

$$N(p) = A' \left( \frac{pc}{1 \text{ MeV}} \right)^{-\Gamma} \exp \left( -\frac{T}{E_{\text{cutoff}}} \right), \quad (49)$$

where  $A'$  has units of  $\text{cm}^{-3} (\text{MeV}/c)^{-1}$  and  $T$  is the kinetic energy. Sturner provided synchrotron, inverse Compton and nonthermal bremsstrahlung spectra for  $\Gamma = 1.8, 2.0$  and  $2.3$  and  $E_{\text{cutoff}} = 10$  TeV. The synchrotron spectrum was computed using  $B_{\text{tot}} = 1 \mu\text{G}$ . The inverse Compton spectrum was computed for the cosmic background radiation field, using a temperature of 2.7 K. The nonthermal bremsstrahlung spectrum was computed for a fully ionized target with ion density  $0.11 \text{ cm}^{-3}$  consisting of protons ( $0.1 \text{ cm}^{-3}$ ), alpha-particles ( $0.01 \text{ cm}^{-3}$ ), and free electrons ( $0.12 \text{ cm}^{-3}$ ), corresponding to relative weights of  $X_e = 1.090$  and  $X_i = 1.182$ , for electron-electron and electron-ion bremsstrahlung, respectively. We used our models to compute photon spectra for the same parameters and particle distribution function.

Figures 4 and 5 show our spectra divided by those obtained from Sturner. Over most of the energy range, our spectra agree quite well with Sturner's; the inverse Compton and synchrotron spectra agree to within  $< 1\%$ , while the nonthermal bremsstrahlung spectra typically differ by  $\lesssim 5\%$ . Aside from the weak  $\Gamma$  dependence in the nonthermal bremsstrahlung differences below about 100 MeV, the differences between Sturner's spectra and ours are largely independent of the spectral index,  $\Gamma$ . Because the  $\Gamma$  dependent errors in our spectra are constrained by the recurrence relation, the weak residual  $\Gamma$  dependence seen in the nonthermal bremsstrahlung differences appears to be associated with Sturner's spectra. The reason for the overall  $\sim 6\%$  discrepancy below 0.25 MeV is unclear; features in the nonthermal bremsstrahlung ratio near 30 TeV and near 10 MeV correspond to points in Sturner's spectra at which the slope

<sup>1</sup> Equation (2.88) of Blumenthal & Gould (1970) involves a constant,  $C_l$ , that is defined in terms of an infinite series that converges extremely slowly:  $C_l \equiv (6/\pi^2) \sum_{k=1}^{\infty} \ln k/k^2 \approx 0.5700$ . From its series definition, it follows that this constant is equivalent to  $C_l = -(6/\pi^2) \zeta'(2)$ , where  $\zeta'$  is the first derivative of the Riemann zeta function. To enable more precise quantitative comparison with the analytic solution, we used the numerical value  $C_l = 0.56996099309453280$ , obtained using the symbolic algebra package MAPLE.

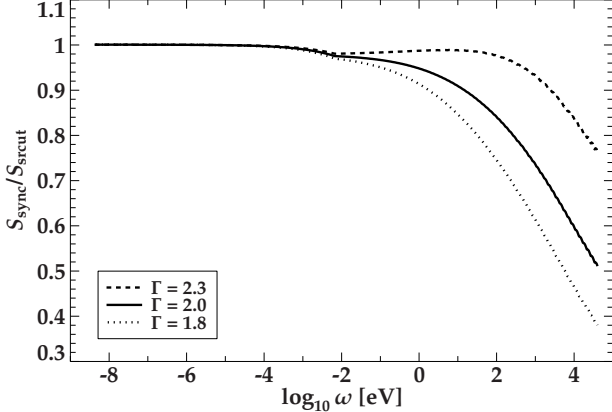


FIG. 6.— Ratio showing our synchrotron fluxes divided by SRCUT synchrotron fluxes from XSPEC for  $\Gamma = 1.8$  (dotted),  $\Gamma = 2$  (solid),  $\Gamma = 2.3$  (dashed). We used  $B_{\text{tot}} = 10 \mu\text{G}$  and  $E_{\text{cutoff}} = 10 \text{ TeV}$  corresponding to  $\nu_{\text{break}} = 1.612 \times 10^{16} \text{ Hz}$ .

changes discontinuously. Because Sturmer's synchrotron and inverse Compton fluxes become negative at the extreme end of the high-energy photon spectra, rather than asymptotically approaching zero as ours do, we attribute the larger differences near the cutoff in these spectra to numerical errors in Sturmer's spectra. However, since the largest differences occur at extremely low flux levels, they are probably not important for observational comparisons.

We also compared our synchrotron model with the SRCUT model (Reynolds 1998; Reynolds & Keohane 1999) in XSPEC version 11.3.2d. SRCUT is designed to compute the synchrotron spectrum from an exponentially cut off power-law distribution of electrons in a homogeneous magnetic field. It depends on a break-frequency parameter,  $\nu_{\text{break}}$ , defined as the critical frequency for  $\sin \alpha = 1$  and  $\gamma \equiv E_{\text{cutoff}}/(m_e c^2)$ . For  $\nu \ll \nu_{\text{break}}$ , we verified that SRCUT is consistent with the analytic result for a power-law electron distribution. For frequencies comparable to  $\nu_{\text{break}}$  or larger, we find that SRCUT spectra differ from our spectra by as much as a factor of two or more. Figure 6 shows that the ratio of the two models depends on photon energy and on the power-law index. The ratio also depends on the break frequency in the sense that the models agree for  $\nu \ll \nu_{\text{break}}$  but disagree for frequencies near the break and above. We are confident that our computed synchrotron spectrum is accurate, first, because the validity of equation (45) indicates that any errors are independent of the power-law index,  $\Gamma$ , and cutoff-energy,  $E_{\text{cutoff}}$  and, second, because our computed spectrum is consistent with Sturmer's model. We conclude that, for frequencies near and above  $\nu_{\text{break}}$ , the SRCUT model does not accurately represent the synchrotron spectrum from an exponentially cut-off power-law distribution of electrons in a homogeneous magnetic field.

We tested our neutral-pion decay model by comparing our results with the results of Mori (1997). For the purpose of this comparison, we used his proton momentum distribution function of the form  $N(p) = (4\pi/v) J_p(p)$

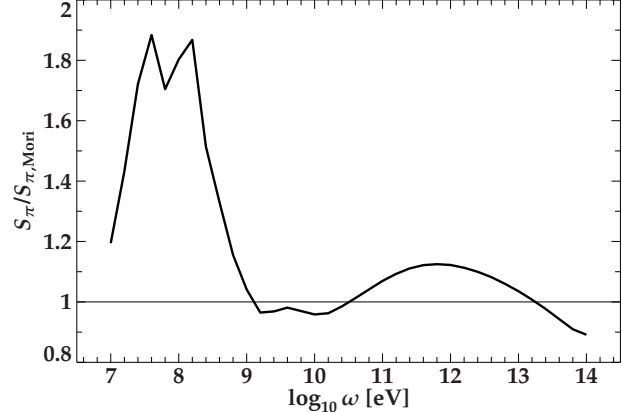


FIG. 7.— Ratio showing our neutral-pion decay spectrum divided by that of Mori (1997).

where

$$J_p(p) = \begin{cases} 6.65 \times 10^{-6} \left( \frac{E}{100 \text{ GeV}} \right)^{-2.75}, & E > 100 \text{ GeV}; \\ 1.67 \left( \frac{p}{\text{GeV}/c} \right)^{-2.7} \left[ 1 + \left( \frac{2.5 \text{ GeV}/c}{p} \right)^2 \right]^{-1/2}, & E \leq 100 \text{ GeV}, \end{cases} \quad (50)$$

where  $p \equiv \gamma m_p v$  and  $E = T + m_p c^2$ . Figure 7 shows our computed neutral-pion decay gamma-ray spectrum divided by the fluxes given in Table 1 of Mori (1997). The largest difference occurs near 100 MeV, where our flux is about a factor of two larger than that of Mori. Because Mori (1997) used a much more detailed model of pion production, we do not expect exact agreement. Yet, for photon energies above 1 GeV, the two gamma-ray fluxes agree to within about 10%. Because we are primarily interested in fitting data in the 1-10 TeV band, our simplified pion-decay model is adequate for our needs.

## 8. FITTING OBSERVED SPECTRA

Fitting a model to an observed spectrum involves minimizing a goodness-of-fit statistic that compares the observed spectral data to the spectral model. This comparison often involves binned data.

For example, consider X-ray observations which provide the observed number of counts in each energy bin. Neglecting nonlinear effects in the X-ray detector, the expected number of counts is usually computed using an expression of the form (Davis 2001)

$$C(h) = B(h) + t \int_{\Delta E_h} dE R(h, E) A(E) S(E), \quad (51)$$

where  $C(h)$  is the total number of counts in bin  $h$ ,  $B(h)$  is the number of counts due to the instrumental background,  $t$  is the exposure time and  $S(E)$  is the spectral model describing the incident flux of photons with energy  $E$ . In equation (51),  $R(h, E)$  is the redistribution function, describing the probability that incident photons with energy  $E$  contribute counts to bin  $h$ , and  $A(E)$  is the effective area, accounting for the telescope collecting area, the transmission efficiency of the optical system and the quantum efficiency of the detector.

In spectral fitting software, equation (51) is usually implemented as a discrete sum of the form

$$C_h = B_h + t \sum_k R_{h,k} A_k S_k. \quad (52)$$

The redistribution function,  $R(h, E)$ , is represented as a matrix,  $R_{h,k}$ , and the effective area and source models are represented as vectors,  $A_k$ , and  $S_k$ , respectively.

To accurately represent the integral in equation (51), the software must compute the model,  $S_k$ , as an integral

$$S_k(E_k; \Delta E_k) \equiv \int_{\Delta E_k} dE S(E), \quad (53)$$

over the width  $\Delta E_k$  of each spectral bin,  $E_k$ . For binned data, we evaluate these integrals using the well-known Simpson's rule. Although this approach requires three function evaluations per bin, the bin-edge function values may be shared between neighboring bins, reducing the total cost of each spectrum computation by about 30%. This approach is accurate to the extent that a quadratic polynomial is a good approximation to the underlying function,  $S(E)$ , within each spectral bin.

### 9. FIT CONSTRAINTS

When simultaneously fitting radio, X-ray and gamma-ray observations of supernova remnants, the degeneracy of certain fit parameters (§3) and the variety of emission mechanisms in the gamma-ray band may make it difficult to determine a unique set of fit parameters unless additional constraints are available.

Based on reasonably general principles, a number of constraints can sometimes be imposed. For example:

1. When the magnetic field associated with the synchrotron emission is generated primarily by cosmic-ray streaming (Lucek & Bell 2000), the energy density in cosmic-rays should set an upper limit on the magnetic energy density. The corresponding upper limit on the magnetic field strength is

$$B_{\text{tot}} \leq \sqrt{8\pi(\varepsilon_e + \varepsilon_p)}, \quad (54)$$

where  $\varepsilon_e$  and  $\varepsilon_p$  are the energy density in cosmic-ray electrons and protons respectively. Because  $B_{\text{tot}}$  and  $E_{\text{cutoff}}$  are degenerate, introducing an upper limit on  $B_{\text{tot}}$  effectively sets a lower limit on  $E_{\text{cutoff}}$ .

2. If electrons and protons are injected into the accelerator at the same rate, the normalization of the proton momentum distribution  $A_p$  can be fixed by requiring equal densities in nonthermal electrons and protons at some characteristic injection kinetic energy  $T_{\text{inj}} \ll m_e c^2$ :

$$N_e(p_{e,\text{inj}})dp_e = N_p(p_{p,\text{inj}})dp_p. \quad (55)$$

When both distribution functions are of the form  $N(p) = A(p/p_0)^{-\Gamma}$  and share the same power-law exponent,  $\Gamma$ , this constraint implies that  $A_p/A_e = (m_p/m_e)^{(\Gamma-1)/2} \approx 91$  if  $\Gamma = 2.2$  (Bell 1978). By fixing the ratio  $A_p/A_e$ , this constraint reduces the variation in the ratio  $\mathcal{N}_\pi/\mathcal{N}_B$  to the variation associated with the mass ratio of the associated targets,  $n_p V_\pi / (n_0 V_B)$ .

3. In many cases it should be reasonable to assume that the emitting volume that produces synchrotron emission will also produce inverse Compton emission due to up-scattering of cosmic background photons. In such cases, one can impose a lower limit on the normalization associated with this inverse Compton process so that  $\mathcal{N}_{I,\text{CBR}} \geq \mathcal{N}_S$ . This constraint ensures that fits to the gamma-ray spectrum will include an appropriate contribution of inverse Compton emission. A similar argument can be used to constrain the minimum value of the nonthermal bremsstrahlung normalization,  $\mathcal{N}_B$  for an assumed minimum target density.

To support imposing constraints based on charge conservation, our software provides a function to compute the proton norm,  $A_p$ , that, for a given electron norm,  $A_e$ , will yield equal nonthermal electron and proton densities at a given injection kinetic energy  $T_{\text{inj}}$ . For constraints that depend on the energy density in nonthermal particles, our software provides functions that compute the energy density of each particle population. The energy density is defined to be

$$\varepsilon = mc^2 \int_{p_{\text{min}}}^{\infty} dp N(p) (\gamma(p) - 1), \quad (56)$$

where the lower integration limit,  $p_{\text{min}}$ , is the momentum at which the thermal and nonthermal particle densities are equal. Note that  $p_{\text{min}}$  depends on the density and temperature of the thermal particles and on the nonthermal particle momentum distribution.

In practice, complicated fit constraints such as the upper limit on  $B_{\text{tot}}$  may be imposed using a technique analogous to the method of Lagrange multipliers (Mathews & Walker 1965). Rather than minimizing  $\chi^2$ , the idea is to construct a constraint function  $g(\mathbf{x}) \geq 0$  which may depend on a vector of parameters,  $\mathbf{x}$ , and then to minimize the sum,  $\chi^2 + \lambda g(\mathbf{x})$ , where  $\lambda$  is a parameter that determines the importance of the constraint. The constraint function should be constructed to ensure that  $g(\mathbf{x}) = 0$  when the constraint is satisfied. For example, to impose the constraint that  $B_{\text{tot}}^2 < 8\pi(\varepsilon_e + \varepsilon_p)$ , one might choose

$$g(\mathbf{x}) = \begin{cases} B_{\text{tot}}^2 [8\pi(\varepsilon_e + \varepsilon_p)]^{-1}, & B_{\text{tot}}^2 \geq 8\pi(\varepsilon_e + \varepsilon_p); \\ 0, & \text{otherwise.} \end{cases} \quad (57)$$

Similar terms may be added to impose additional constraints.

### 10. CONCLUSIONS

We have described models that can be used to compute the synchrotron, inverse Compton, nonthermal bremsstrahlung and neutral-pion decay spectra of homogeneous sources containing nonthermal electrons and protons. We have implemented these models as an importable module for use in the spectral fitting package *ISIS* (Houck & Denicola 2000); the software is available from the *ISIS* web page<sup>2</sup>. The models are designed to be accurate and fast enough for use in interactive data analysis on a typical workstation. To the best of our knowledge, this is the first implementation of some of these models in a form suitable for interactive fitting with

<sup>2</sup> <http://space.mit.edu/cxc/isis>

publicly available data analysis software. Results derived using the synchrotron and inverse Compton models have been presented elsewhere by Pannuti et al. (2003) and by Allen, Houck & Sturmer (2005).

We assessed the accuracy of these models by using a recurrence relation, by comparing with analytic solutions for synchrotron and inverse Compton scattering and by comparing with published work by other authors. The accuracy with which our solutions obey the recurrence relation in equation (46) demonstrates their correct dependence upon the power-law index and cutoff-energy parameters. We also showed that, over most of the energy range of interest, our models agree with those of Sturmer et al. (1997). The largest differences between our models and those of Sturmer et al. (1997), of order  $\sim 10\%$ , occur near the cutoff of each model spectrum and are essentially independent of the spectral index.

We found much larger differences between our synchrotron spectrum and the SRCUT model from XSPEC. Although consistent with the analytic solution for  $\nu \ll \nu_{\text{break}}$ , SRCUT differs from our model and from Sturmer's by as much as a factor of two or more in the X-ray band near  $\nu_{\text{break}}$  (see Figure 6). The most important difference is that the normalization derived using SRCUT overestimates the radio flux at 1 GHz by an amount dependent upon the spectral index as shown in Figure 6. The spec-

tral index from SRCUT tends to be a few percent too steep and the break frequency tends to be a few percent too low but, in practice, such differences may be detectable only with very high quality data. Note that, by overestimating the radio flux, SRCUT may suggest the existence of positive curvature in the underlying particle momentum distribution.

In future work, we hope to improve the neutral-pion decay model by explicitly computing the integral over proton momenta using improved pion-production cross-sections. This refinement will extend the applicable range to sub-GeV photon energies and will improve the overall accuracy of the model. These improvements will be more important as better observations of the gamma-ray spectrum become available from the *Gamma-Ray Large Area Space Telescope* (GLAST)<sup>3</sup> and from future advances in instrumentation.

We thank E. Haug for providing software to compute values for the electron-electron bremsstrahlung cross-sections and S. Sturmer for providing numerical tables used to verify our results for selected electron momentum distributions. We also acknowledge useful conversations with John E. Davis and a number of comments from the referee which helped us to improve the paper.

<sup>3</sup> <http://glast.gsfc.nasa.gov>

## APPENDIX

### A. SPECTRUM TABLES

For reference, Tables B1, B2 and B3 contain sample spectra for each emission process described in this paper. The nonthermal electron and proton momentum spectra have the same shape, with slope  $\Gamma = 2$ , and a cutoff energy  $E_{\text{cutoff}} = 10 \text{ TeV}$ . Table B1 gives synchrotron spectra for curvatures  $a = 0$  and  $a = 0.05$ . Tables B2 and B3 give the inverse Compton, nonthermal bremsstrahlung and neutral-pion decay spectra for curvatures  $a = 0$  and  $a = 0.05$ , respectively. All normalization coefficients were set to unity. The synchrotron spectrum was computed for  $B_{\text{tot}} = 10 \mu\text{G}$ . The inverse Compton spectrum was computed using a 2.725 K blackbody distribution of seed photons (Bennett et al. 2003). Contributions to nonthermal bremsstrahlung due to the electron-electron and electron-proton processes are listed separately, with their respective weights set to unity.

### B. DISTRIBUTED COMPUTATION

The spectral models described in this paper were designed to fit multi-wavelength spectral data interactively on a typical workstation and to achieve a high degree of accuracy as efficiently as possible. In practice, to be sure that the fit has fully converged and to derive confidence limits, it is necessary to thoroughly examine the parameter space in the neighborhood of the best-fit parameters. To conduct this search more quickly, we have found it useful to distribute the task of computing single-parameter confidence limits over a number processors running in parallel (Noble et al. 2005). One master process manages the computations being performed by a number of slave processes that run on different computers. All of the computers are connected by a local network and all processes have access to the relevant data and spectral models. The master process assigns each slave process the task of computing confidence limits for a single parameter. If a slave process finds an improved fit, that new parameter set is sent to the master process. If that fit is the best yet found by any slave, the master commands all the slave processes to re-start the search from the beginning, using the new parameter set. We have found that the time required to obtain a set of converged single parameter confidence limits using this approach is often reduced by more than a factor of  $N$ , where  $N$  is the number of slave processes.

We have implemented this algorithm using the Parallel Virtual Machine (PVM) (Geist et al. 1994) to handle message passing between the master and slave processes. We used the spectral fitting package, ISIS (Houck & Denicola 2000) to perform model fits and confidence limit searches using a set of S-Lang scripts. An S-Lang module provides a scriptable interface to the PVM library, making it possible for these scripts to communicate with the PVM.

TABLE B1  
SAMPLE SYNCHROTRON SPECTRA

Energy (eV)	Flux		Energy (eV)	Flux	
	a=0 (photons s <sup>-1</sup> cm <sup>-2</sup> GeV <sup>-1</sup> )	a=0.05 (photons s <sup>-1</sup> cm <sup>-2</sup> GeV <sup>-1</sup> )		a=0 (photons s <sup>-1</sup> cm <sup>-2</sup> GeV <sup>-1</sup> )	a=0.05 (photons s <sup>-1</sup> cm <sup>-2</sup> GeV <sup>-1</sup> )
1.0000e-07	6.8294e+15	6.8613e+15	1.7783e-01	2.5564e+06	7.0374e+06
1.7783e-07	2.8798e+15	2.9011e+15	3.1623e-01	1.0403e+06	3.1004e+06
3.1623e-07	1.2144e+15	1.2284e+15	5.6234e-01	4.1918e+05	1.3546e+06
5.6234e-07	5.1206e+14	5.2114e+14	1.0000e+00	1.6680e+05	5.8530e+05
1.0000e-06	2.1591e+14	2.2168e+14	1.7783e+00	6.5346e+04	2.4928e+05
1.7783e-06	9.1040e+13	9.4594e+13	3.1623e+00	2.5107e+04	1.0423e+05
3.1623e-06	3.8386e+13	4.0507e+13	5.6234e+00	9.4173e+03	4.2578e+04
5.6234e-06	1.6184e+13	1.7409e+13	1.0000e+01	3.4291e+03	1.6897e+04
1.0000e-05	6.8229e+12	7.5091e+12	1.7783e+01	1.2040e+03	6.4693e+03
1.7783e-05	2.8762e+12	3.2506e+12	3.1623e+01	4.0433e+02	2.3701e+03
3.1623e-05	1.2123e+12	1.4121e+12	5.6234e+01	1.2859e+02	8.2272e+02
5.6234e-05	5.1092e+11	6.1560e+11	1.0000e+02	3.8275e+01	2.6741e+02
1.0000e-04	2.1528e+11	2.6929e+11	1.7783e+02	1.0511e+01	8.0233e+01
1.7783e-04	9.0683e+10	1.1819e+11	3.1623e+02	2.6180e+00	2.1844e+01
3.1623e-04	3.8186e+10	5.2042e+10	5.6234e+02	5.7921e-01	5.2861e+00
5.6234e-04	1.6072e+10	2.2985e+10	1.0000e+03	1.1101e-01	1.1090e+00
1.0000e-03	6.7607e+09	1.0181e+10	1.7783e+03	1.7883e-02	1.9570e-01
1.7783e-03	2.8416e+09	4.5213e+09	3.1623e+03	2.3343e-03	2.8009e-02
3.1623e-03	1.1931e+09	2.0124e+09	5.6234e+03	2.3621e-04	3.1107e-03
5.6234e-03	5.0025e+08	8.9740e+08	1.0000e+04	1.7564e-05	2.5414e-04
1.0000e-02	2.0938e+08	4.0070e+08	1.7783e+04	8.9943e-07	1.4316e-05
1.7783e-02	8.7436e+07	1.7903e+08	3.1623e+04	2.9327e-08	5.1409e-07
3.1623e-02	3.6404e+07	7.9973e+07	5.6234e+04	5.5363e-10	1.0702e-08
5.6234e-02	1.5099e+07	3.5680e+07	1.0000e+05	5.3930e-12	1.1512e-10
1.0000e-01	6.2322e+06	1.5878e+07	1.7783e+05	2.3578e-14	5.5658e-13

TABLE B2  
SAMPLE GAMMA-RAY SPECTRA ( $a = 0$ )

Energy (eV)	Inv. Comp.	Flux		
		ee Brem. (photons s <sup>-1</sup> cm <sup>-2</sup> GeV <sup>-1</sup> )	ep Brem. (photons s <sup>-1</sup> cm <sup>-2</sup> GeV <sup>-1</sup> )	$\pi^0$ decay
1.0000e+06	2.0062e-10	1.3845e-10	1.6562e-10	8.2454e-18
1.7783e+06	8.4541e-11	5.3800e-11	6.2697e-11	2.4513e-17
3.1623e+06	3.5616e-11	2.0632e-11	2.3393e-11	7.0967e-17
5.6234e+06	1.5000e-11	7.7773e-12	8.5860e-12	1.9707e-16
1.0000e+07	6.3147e-12	2.8778e-12	3.1021e-12	5.1353e-16
1.7783e+07	2.6568e-12	1.0460e-12	1.1053e-12	1.2201e-15
3.1623e+07	1.1170e-12	3.7410e-13	3.8916e-13	2.5548e-15
5.6234e+07	4.6913e-13	1.3195e-13	1.3565e-13	2.7122e-15
1.0000e+08	1.9677e-13	4.6000e-14	4.6881e-14	2.7122e-15
1.7783e+08	8.2389e-14	1.5880e-14	1.6085e-14	1.9824e-15
3.1623e+08	3.4416e-14	5.4375e-15	5.4842e-15	9.0019e-16
5.6234e+08	1.4332e-14	1.8492e-15	1.8596e-15	3.6492e-16
1.0000e+09	5.9441e-15	6.2516e-16	6.2745e-16	1.3641e-16
1.7783e+09	2.4521e-15	2.1026e-16	2.1075e-16	4.8273e-17
3.1623e+09	1.0045e-15	7.0378e-17	7.0481e-17	1.6490e-17
5.6234e+09	4.0771e-16	2.3445e-17	2.3468e-17	5.5070e-18
1.0000e+10	1.6351e-16	7.7725e-18	7.7775e-18	1.8116e-18
1.7783e+10	6.4567e-17	2.5626e-18	2.5637e-18	5.8906e-19
3.1623e+10	2.4988e-17	8.3928e-19	8.3953e-19	1.8934e-19
5.6234e+10	9.4223e-18	2.7251e-19	2.7257e-19	5.9973e-20
1.0000e+11	3.4360e-18	8.7461e-20	8.7476e-20	1.8582e-20
1.7783e+11	1.2001e-18	2.7620e-20	2.7624e-20	5.5578e-21
3.1623e+11	3.9651e-19	8.5250e-21	8.5262e-21	1.5693e-21
5.6234e+11	1.2191e-19	2.5465e-21	2.5469e-21	4.0316e-22
1.0000e+12	3.4130e-20	7.2548e-22	7.2560e-22	8.8745e-23
1.7783e+12	8.4456e-21	1.9286e-22	1.9290e-22	1.5161e-23
3.1623e+12	1.7719e-21	4.6256e-23	4.6267e-23	1.7037e-24
5.6234e+12	2.9674e-22	9.4868e-24	9.4896e-24	9.4934e-26
1.0000e+13	3.6207e-23	1.5226e-24	1.5232e-24	1.6037e-27
1.7783e+13	2.7845e-24	1.6433e-25	1.6443e-25	3.4422e-30
3.1623e+13	1.0582e-25	9.1509e-27	9.1588e-27	1.9973e-34
5.6234e+13	1.2918e-27	1.6454e-28	1.6477e-28	1.9824e-41
1.0000e+14	2.3039e-30	4.1544e-31	4.1640e-31	2.4571e-53

TABLE B3  
SAMPLE GAMMA-RAY SPECTRA ( $a = 0.05$ )

Energy (eV)	Inv. Comp.	Flux		
		$ee$ Brem. (photons $s^{-1}$ $cm^{-2}$ $GeV^{-1}$ )	$ep$ Brem. ( $cm^{-2}$ $GeV^{-1}$ )	$\pi^0$ decay
1.0000e+06	2.4116e-10	1.3856e-10	1.6572e-10	1.1455e-17
1.7783e+06	1.0553e-10	5.3856e-11	6.2750e-11	3.1243e-17
3.1623e+06	4.6340e-11	2.0662e-11	2.3422e-11	8.4245e-17
5.6234e+06	2.0415e-11	7.7932e-12	8.6015e-12	2.2119e-16
1.0000e+07	9.0225e-12	2.8864e-12	3.1106e-12	5.5285e-16
1.7783e+07	3.996e-12	1.0506e-12	1.1099e-12	1.2763e-15
3.1623e+07	1.7779e-12	3.7663e-13	3.9168e-13	2.6248e-15
5.6234e+07	7.9236e-13	1.3332e-13	1.3701e-13	2.7832e-15
1.0000e+08	3.5389e-13	4.6739e-14	4.7619e-14	2.7832e-15
1.7783e+08	1.5832e-13	1.6278e-14	1.6483e-14	2.0479e-15
3.1623e+08	7.0899e-14	5.6505e-15	5.6971e-15	9.5028e-16
5.6234e+08	3.1756e-14	1.9621e-15	1.9725e-15	3.9827e-16
1.0000e+09	1.4211e-14	6.8424e-16	6.8653e-16	1.5601e-16
1.7783e+09	6.3444e-15	2.4051e-16	2.4101e-16	5.8712e-17
3.1623e+09	2.8206e-15	8.5278e-17	8.5385e-17	2.1653e-17
5.6234e+09	1.2459e-15	3.0488e-17	3.0513e-17	7.9260e-18
1.0000e+10	5.4508e-16	1.0983e-17	1.0988e-17	2.9006e-18
1.7783e+10	2.3532e-16	3.9805e-18	3.9818e-18	1.0644e-18
3.1623e+10	9.9771e-17	1.4483e-18	1.4486e-18	3.9144e-19
5.6234e+10	4.1292e-17	5.2743e-19	5.2752e-19	1.4370e-19
1.0000e+11	1.6555e-17	1.9143e-19	1.9145e-19	5.2220e-20
1.7783e+11	6.3677e-18	6.8852e-20	6.8859e-20	1.8516e-20
3.1623e+11	2.3209e-18	2.4353e-20	2.4355e-20	6.2578e-21
5.6234e+11	7.8871e-19	8.3813e-21	8.3822e-21	1.9414e-21
1.0000e+12	2.4462e-19	2.7658e-21	2.7661e-21	5.2052e-22
1.7783e+12	6.7266e-20	8.5667e-22	8.5679e-22	1.0934e-22
3.1623e+12	1.5746e-20	2.4116e-22	2.4121e-22	1.5278e-23
5.6234e+12	2.9588e-21	5.8625e-23	5.8639e-23	1.0730e-24
1.0000e+13	4.0826e-22	1.1297e-23	1.1301e-23	2.3213e-26
1.7783e+13	3.5900e-23	1.4881e-24	1.4888e-24	6.4948e-29
3.1623e+13	1.5844e-24	1.0307e-25	1.0315e-25	5.0034e-33
5.6234e+13	2.2946e-26	2.3534e-27	2.3565e-27	6.7148e-40
1.0000e+14	4.9900e-29	7.7046e-30	7.7217e-30	1.1451e-51

## REFERENCES

Aharonian, F. A., & Atoyan, A. M., 2000, A&A, 362, 937

Allen, G. E., Houck, J. C., & Sturmer, S. J., 2005, in X-Ray and Radio Connections (eds. L.O. Sjouwerman and K.K. Dyer) Published electronically by NRAO, <http://www.aoc.nrao.edu/events/xraydio>

Baring, M. G., Ellison, D. C., Reynolds, S. P., Grenier, I. A., & Goret, P., 1999, ApJ, 513, 311

Bell, A. R., 1978, MNRAS, 182, 443

Bell, A. R., 1987, MNRAS, 225, 615

Bennett, C. L., et al., 2003, ApJS, 148, 1

Berezhko, E. G., & Ellison, D. C., 1999, ApJ, 526, 385

Blandford, R., & Eichler, D., 1987, Phys. Rep., 154, 1

Blumenthal, G. R., & Gould, R. J., 1970, Reviews of Modern Physics, 42, 237

Bykov, A. M., Chevalier, R. A., Ellison, D. C., & Uvarov, Y. A., 2000, ApJ, 538, 203

Crusius, A., & Schlickeiser, R., 1986, A&A, 164, L16

Davis, J. E., 2001, ApJ, 548, 1010

de Boor, C., 1978, A Practical Guide to Splines, (New York: Springer)

Dermer, C. D., 1986, A&A, 157, 223

Ellison, D. C., & Reynolds, S. P., 1991, ApJ, 382, 242

Elwert, G., 1939, Ann. Phys., 34, 178

Gaisser, T., 1994, Cosmic Rays and Particle Physics, (Cambridge: Cambridge Univ. Press)

Galassi, M., Davies, J., Theiler, J., Gough, B., Jungman, B., Booth, M., & Rossi, F., 2005, GNU Scientific Library Reference Manual - Revised Second Edition, (Bristol: Network Theory Ltd)

Geist, A., Beguelin, A., Dongarra, J., Weicheng, J., Manchek, R., & Sunderam, V., 1994, PVM: Parallel Virtual Machine: A Users' Guide and Tutorial for Networked Parallel Computing, (Boston: MIT Press)

Haug, E., 1975, Z. Naturforsch., 30a, 1099

Haug, E., 1997, A&A, 326, 417

Heitler, W., 1953, The Quantum Theory of Radiation, 3rd ed., (New York: Dover)

Hillier, R., 1984, Gamma Ray Astronomy, (Oxford: Clarendon)

Houck, J. C., & Denicola, L. A., 2000, in ASP Conf. Ser. 216: Astronomical Data Analysis Software and Systems IX, 591

Jones, T. J., Rudnick, L., DeLaney, T., & Bowden, J., 2003, ApJ, 587, 227

Koch, H. W., & Motz, J. W., 1959, Reviews of Modern Physics, 31, 920

Landau, L. D., & Lifshitz, E. M., 1975, The Classical Theory of Fields, (Oxford: Pergamon)

Lucek, S. G., & Bell, A. R., 2000, MNRAS, 314, 65

Mathews, J., & Walker, R., 1965, Mathematical Methods of Physics, (New York: Benjamin)

Mori, M., 1997, ApJ, 478, 225

Noble, M. S., Houck, J. C., Davis, J. E., Young, A., & Nowak, M., 2005, in ASP Conf. Ser.: Astronomical Data Analysis Software and Systems XV

Pannuti, T. G., Allen, G. E., Houck, J. C., & Sturmer, S. J., 2003, ApJ, 593, 377

Pratt, R. H., & Tseng, H. K., 1975, Phys. Rev. A, 11, 1797

Reynolds, S. P., 1998, ApJ, 493, 375

Reynolds, S. P., & Keohane, J. W., 1999, ApJ, 525, 368

Sturmer, S. J., Skibo, J. G., Dermer, C. D., & Mattox, J. R., 1997, ApJ, 490, 619

*Note added in proof.*—After this manuscript was submitted, papers by Kamae *et al.* (astro-ph/0605581) and by Kelner, Aharonian & Bugayov (astro-ph/0606058) appeared, presenting parameterized cross-sections for various particles produced of  $pp$  collisions. We plan to revise our pion-decay model to incorporate these new cross-sections. Details will be discussed in a subsequent paper.